

Article

Study of the Subsidence Width Influence on the Geotextile Control of a Subgrade Collapse Based on a Half-Symmetric Model Test

Di Wu, Yihuai Liang, Yanxin Yang *  and Jianjian Wu

School of Architecture and Transportation Engineering, Guilin University of Electronic Technology, Guilin 541004, China

* Correspondence: yanxinyangswjtu@foxmail.com

Abstract: The geotextile can be used to treat a subgrade collapse in karst areas. The subsidence width is an important factor affecting the geotextile to treat subgrade collapses. However, the available studies on the influence of the subsidence width on geotextile treatment settlement are limited. To study the effect of the subsidence width on the geotextile control of subgrade collapses, the half-symmetric model test had been established. To make up for the deficiencies of the model test, the optimized subsidence width was probed through a numerical calculation under ten different situations conducted by the finite element analyses. Previous full-section model test results were used to verify the rationality of the half-symmetric model and calibrate the input parameters of the numerical models. The influence of the subsidence width on soil pressure, tensile force and deformation of the geotextile, and soil settlement was analyzed. With the increase of the subsidence width, more loads of the subsidence area were transferred to a stable area via the geotextile, the vertical normal stress at the edge increased rapidly, the tensile force of the geotextile and vertical soil displacement in the subsidence area increased noticeably. When the anchorage ratio of $L \leq 2.0B$, the geotextile fracture or soil failure occurred during the model test which indicated the geotextile treatment of the subgrade collapse was not suitable for projects with an anchorage ratio of $L \leq 2.0B$. The geotextile might be reaching the limit of its tensile stiffness when the anchorage ratio of $L = 2.22B$. This is providing an insight into the treatment of a subgrade collapse in karst areas using geotextile.

Keywords: geotextile; half-symmetric model; model test; subsidence width; numerical modeling



Citation: Wu, D.; Liang, Y.; Yang, Y.; Wu, J. Study of the Subsidence Width Influence on the Geotextile Control of a Subgrade Collapse Based on a Half-Symmetric Model Test. *Appl. Sci.* **2022**, *12*, 9504. <https://doi.org/10.3390/app12199504>

Academic Editors: Xiaowu Tang and Chao Xu

Received: 1 September 2022

Accepted: 19 September 2022

Published: 22 September 2022

Publisher's Note: MDPI stays neutral with regard to jurisdictional claims in published maps and institutional affiliations.



Copyright: © 2022 by the authors. Licensee MDPI, Basel, Switzerland. This article is an open access article distributed under the terms and conditions of the Creative Commons Attribution (CC BY) license (<https://creativecommons.org/licenses/by/4.0/>).

1. Introduction

A subgrade collapse in karst areas poses a great threat to the operation of road, railway, and to the safety of the inhabitants [1–8]. The size of the subgrade collapse in karst areas could vary from several to thousands of square meters. To control a subgrade collapse, geosynthetics had been used as in-situ treatments for a subgrade collapse in the karst areas [9–13], thereby improving the stability of the soil structure. Studies using other novel materials are conducted to control a subgrade collapse, for example, Rehman and Khalid Geogrids [14,15] used COVID-19 face mask waste fibers and silica fumes to ameliorate mechanical properties of fat clay.

Geosynthetics, geogrids, geomembranes, non-woven fabrics, and other alternatives were often used as reinforcement materials in most cases, however, the use of geotextile as a reinforcement material has received more attention due to its great performance. It was found that the application of geosynthetics were affected by the subsidence width when treating a subgrade collapse [16–18].

To evaluate the performance of geosynthetics, the mechanical properties are obtained via in-situ and laboratory tests. Tavakoli and Khazaei [19] found the bearing capacity of reinforced soil was 635% higher than that of unreinforced soil by 36 repeated tests under different conditions, and it was concluded that the optimum aperture size of the geogrids

should be 0.2 times width of the foundation. To survey the condition of reinforced soil embankments under hollow conditions, circular cavity tests with diameters of 0.75 m, 1.25 m, and 2.2 m were carried by Huckert et al. [20]. The experiments showed that the tensile force of the geosynthetic located over and around the cavity in the anchorage areas, the shape of the geosynthetic was parabolic. Eekelen et al. [21] conducted 12 groups of laboratory model tests on pile embankments and analyzed the relationship between the load distribution and the geosynthetic deformation, and discovered that the load of geosynthetics mainly concentrated on strips between piles and adjacent piles and around pile caps. Chawla and Shahu [22] conducted model tests of tracks that were reinforced with a geogrid or a geotextile and laid on two different subgrade soils, namely, Dhanaury clay and Delhi silt, and discovered that the tracks reinforced with a geotextile performed better with respect to the reduced tie displacement, subgrade displacement and sub ballast strain, compared to the tracks reinforced with a geogrid when Delhi silt was used as the subgrade soil. King et al. [23] used the limit equilibrium model to study the relationship between long-term creep compression and settlement of the geosynthetics reinforced soil foundation, the raised questions about the long-term performance and the manner in which an acceptable performance had been achieved in the short-term in several field case studies. In addition, the numerical simulation can make up the deficiencies of the model test as an alternative research method. Villard et al. [24] studied the mechanical behavior of a geosynthetic reinforced embankment in high-risk subsidence areas by a numerical model, and discovered that the opening mode of the hole had a great influence on the load distribution above the reinforced hole. Huckert et al. [25] explored the shape of the load distribution on the geosynthetics by the numerical simulation based on full-section tests. The authors found that the deduced shape of the load distribution was inverted triangular for a 0.75 m diameter sinkhole and uniform for a 2.2 m diameter cavity, both under a non-cohesive 1 m high embankment. Briançon et al. [26] conducted a numerical study based on the coupling of the finite element method (FEM) and discrete element method (DEM), and found that the data obtained by the new method were consistent with the full-sized test data. Wu et al. [27] observed in the established model by the finite element software that the anchorage length greater than $0.25B$ is required to ensure the stability of structure the increase of the anchorage length of the geotextile could provide a greater tensile force for the geotextile, better control of the soil settlement and improve the soil stability.

The performance of geosynthetics is controlled by the anchorage length and buried depth, while the influence of the subsidence width on the geosynthetics or geotextile were not investigated. This paper explored the effect of the subsidence width on the geotextile treatment of a subgrade collapse by a half-symmetric test model. In addition, the optimized subsidence width was explored with ten different conditions conducted by numerical models to make up for the deficiencies of the model test work. The influence of the subsidence width on soil pressure, tensile force, and deformation of the geotextile, and the settlement were analyzed. Based on the analysis results, the subsidence width for using geotextile controlling a subgrade collapse was obtained.

2. Research Methods

2.1. Model Test

Zhang et al. [28] investigated the symmetry of the embankment, a half-symmetric model was established in a finite element software, and the performance of a fixed-geosynthetic-reinforced and pile-supported embankment (called FGT embankment) was studied. Feng et al. [29] established a half-symmetric centrifugal test model based on the Maputo Bridge and Link Roads Project in Mozambique, and studied the deformation and failure modes of the embankment supported by geogrid reinforced piles. As mentioned above, the test results of the half-symmetric test could represent the variation of analysis results if a full-section test was difficult to establish. Based on Wu et al. [30,31], the large-scale model tests had been conducted with the dimensions of $1.5\text{ m} \times 0.6\text{ m} \times 1.5\text{ m}$ (length \times width \times height). This paper presents a half-symmetric test model based on the

size dimensions of the full-section test conducted by Wu et al. [30,31]. Only a half size of the full-section test was used to build the test model.

Table 1 lists the model tests performed in this paper. According to the prototype size and scale factor $N = 5.0$, the anchorage length L of the geotextile was set as 600 mm in the model test. The tests H1, H2, H3, and H4 represented the test with the subsidence width (denoted as B) of 300 mm, 150 mm, 300 mm, and 600 mm, respectively, which were conducted to research the influence of the subsidence width on the geotextile control of a subgrade collapse. L/B represented the anchorage length of the geotextile L to the subsidence width B .

Table 1. Model test program.

Variation	Test No.	Subsidence Width, B (mm)	Anchorage Length of the Geotextile, L (mm)	Anchorage Ratio, L/B	Buried Depth of the Geotextile, H (mm)
Subsidence width	H1	300	1200	4.0	1000
	H2	150	600	4.0	1000
	H3	300	600	2.0	1000
	H4	600	600	1.0	1000

Figure 1 shows the layout of the half-symmetric model test. In the middle of the model box, the rigid baffle treated was wrapped by a double-layer Teflon film. On the left side of the rigid baffle was the test soil, and on the right side was the rigid support. The rigid baffle was connected with the rigid support and its position could be adjusted. The model geotextile was laid in the rigid stable area. As a comparison, the geotextiles did not fold upwards at the position of rigid baffle in the full-section model test. The geotextile on one side of rigid baffle was folded upwards and extended to contact the movable side plate and fixed with thumbtacks. The test conditions of the different subsidence widths were realized by changing the width of the movable bottom plate. The movable side plate was in contact with the rigid baffle, and the double-layer Teflon film was placed between them. The model geotextile on the rigid baffle side was fixed and the vertical settlement was allowed during the test.

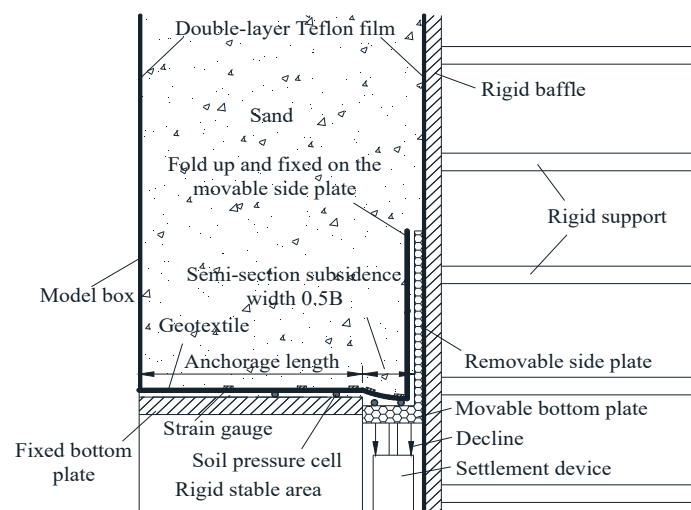


Figure 1. Sketch graph of the geotextile of half-symmetric model.

During the subgrade collapse test, the soil pressure cells were used to record soil stress and the strain gauges recorded the deformation of the geotextile. The settlement of the movable bottom plate was measured with an electromechanical dial indicator. Additionally, the soil settlement within the subsidence area was captured and analyzed with particle image velocimetry (PIV) equipment. All monitoring equipment were connected to the static strain gauge, and the computer collected real-time data once per second. Figure 2a,b

show the model size and layout of the instruments (unit: mm). T represented the soil pressure cell, Y represented the strain gauge, h represented the settlement markers [32]. Figure 2c shows the field test diagram of the half-symmetric model.

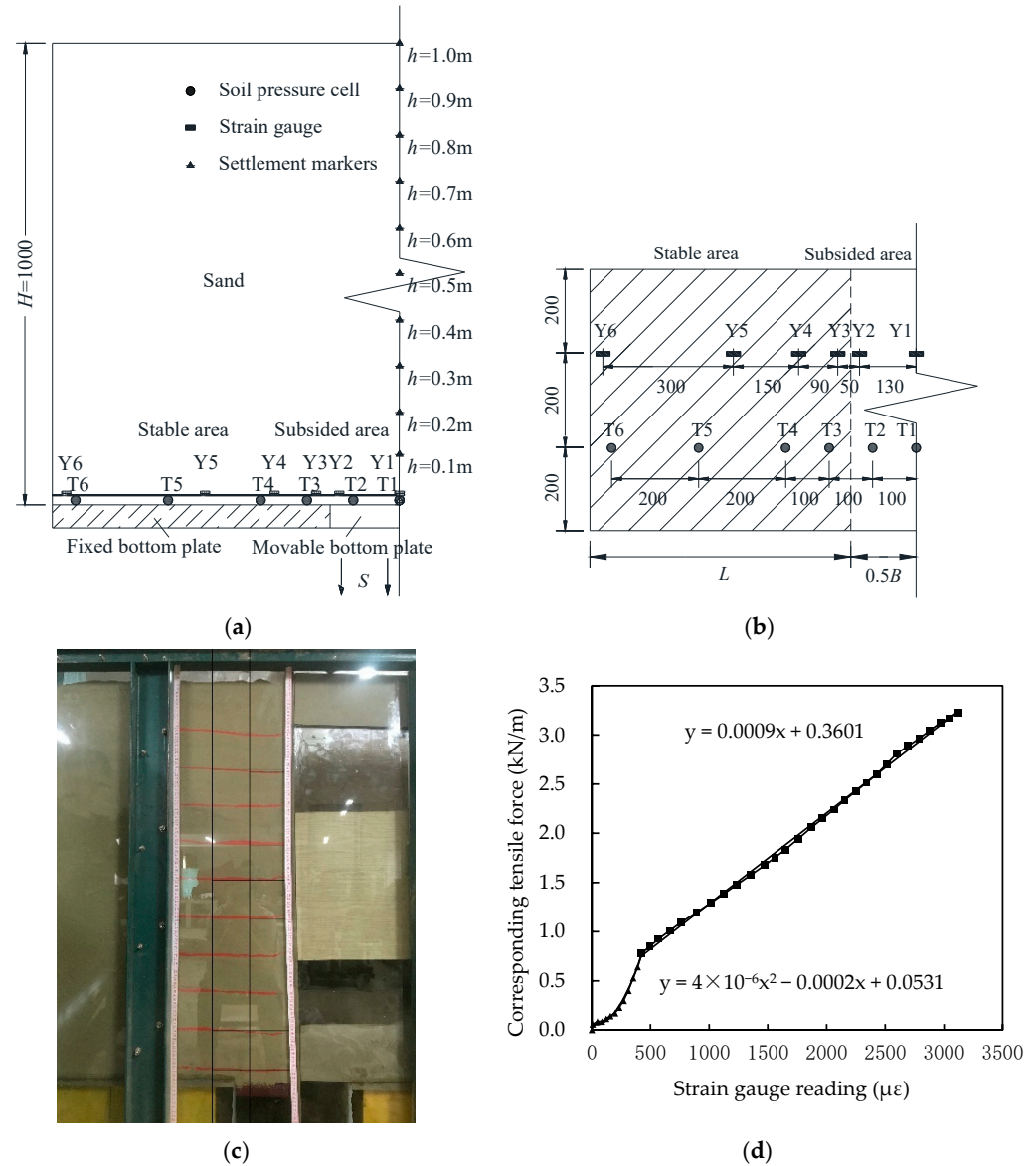


Figure 2. Placement situation of the monitor’s components: (a) vertical graph; (b) plane graph; (c) model test diagram (unit: mm); (d) strain-tensile force-strain curve by the gauge.

The model test used dry Li-River sand in Guilin, and its physical and mechanical parameters are shown in Table 2. The medical gauze was used to simulate geotextiles in the test, based on Wang et al. [33], the physical and mechanical parameters are shown in Table 3.

Table 2. Physical and mechanical parameters of the Li-River sand.

Parameters of Sand	Density, t/m ³	Maximum Dry Density, t/m ³	Moisture Content, %	Internal Friction Angle, °	Cohesion, kPa	Relative Density of Sand, t/m ³
Li-River sand	1.61	1.68	1.03	32.8	0.20	2.63

Table 3. Physical and mechanical parameters of the medical gauze.

Weight of Per Unit Area, g/m ²	Thickness, mm	Tensile Strength, kN/m	Tensile Stiffness, kN/m
60	0.16	3.22	48

2.2. Numerical Modeling

The numerical model was established to simulate the half-symmetric model based on the numerical modeling which was validated by the pre-existing model tests by Wu et al. [27]. In this paper, a half-symmetric numerical model was established to study the influence of the subsidence width on the treatment effect of a subgrade collapse. Figure 3 shows the half-symmetric numerical model with the size of 20 m × 5 m, and the interface strength reduction factor was set as 0.9. The model used 15-node triangular element for meshing, with a total of 4248 elements and 34,517 nodes. The Mohr–Coulomb constitutive model with the drainage condition was used. The soil element used in the numerical model had a unit weight of 17.0 kN/m³, an elastic modulus of 30,000 kN/m², a Poisson’s ratio of 0.3, a cohesion of 1.0 kPa, and an internal friction angle of 33°, respectively. The tensile stiffness of the geotextile in the numerical model was 3000 kN/m. The process of the soil subsidence was simulated using the “linear displacement” in PLAXIS, and the “geogrid” simulated the geotextile, and the model boundary conditions were selected to be fixed in the normal direction.

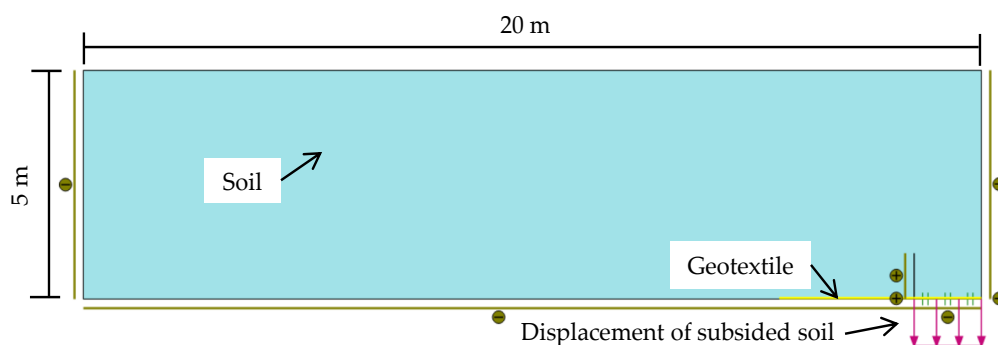


Figure 3. Numerical model.

Table 4 lists the numerical models for the different conditions to study the influence of the subsidence width on the treatment effect of a subgrade collapse. The full-section numerical models denoted as P1–P3 were constructed with the subsidence widths of geotextile B of 1500 mm, 3000 mm, and 6000 mm, respectively. The half-symmetric model denoted as P4–P10 were constructed with the subsidence widths of geotextile B of 750 mm, 900 mm, 1050 mm, 1200 mm, 1350 mm, 1500 mm, and 3000 mm, respectively. The corresponded L/B for the ten models were 4.0, 2.0, 1.0, 4.0, 3.33, 2.86, 2.50, 2.22, 2.0, and 1.0, respectively.

Table 4. Numerical models with various anchorage ratios.

Variation	Numerical Model	Subsidence Width, B (mm)	Anchorage Length of Geotextile, L (mm)	Anchorage Ratio, L/B	Buried Depth of Geotextile, H (mm)	Tensile Stiffness of Geotextile, EA/(kN·m ⁻¹)
Subsidence width	P1	1500	6000	4.0	5000	3000
	P2	3000	6000	2.0	5000	3000
	P3	6000	6000	1.0	5000	3000
	P4	750	3000	4.0	5000	3000
	P5	900	3000	3.33	5000	3000
	P6	1050	3000	2.86	5000	3000
	P7	1200	3000	2.50	5000	3000
	P8	1350	3000	2.22	5000	3000
	P9	1500	3000	2.0	5000	3000
	P10	3000	3000	1.0	5000	3000

3. Experiment Results and Analysis

3.1. Validation of the Half-Symmetric Model and the Numerical Modeling

The rationality of the half-symmetric model and the numerical modeling are validated by analyzing the test results of the half-symmetric model H2 group, the full-section H1 group, the numerical full-section P1 group, and the numerical half-symmetric model P4 group. Figure 4 compares the relationship between the model test and the numerical model results of the half-symmetric model and full-section model at the final state of the subgrade collapse under $L = 4.0B$. Overall, the curve amounts of the subsidence area of the half-symmetric model H2 group, the full-section H1 group, the numerical full-section P1 group, the numerical half-symmetric model P4 group are similar.

Figure 4a shows the soil pressure of groups H1, H2, P1, and P4 when $L = 2.0B$. With the increase of the horizontal distance from the subsidence area, the soil pressure increases rapidly in the stable area. The soil pressure of each curve reaches its peak value at the horizontal distance between 1.5 m and 2.0 m from the subsidence area, and then decreases to the initial earth pressure. This shows that the soil within the subsidence area gradually sinks and the soil of the surrounding stable area moves to the subsidence area with the development of a subgrade collapse, so the compactness of the soil near the subgrade collapse interface decreases and the measure of the earth pressure decreases. When $L = 2.0B$, the soil pressure curve trend of the half-symmetric model H2 group is similar with the full-section H1 group, which indicates the soil pressure test results of the half-symmetric model can represent the soil pressure data of the full-section model test. The validity of the numerical model is proved by the approximate similar curve trends obtained from the model test and the numerical models.

Figure 4b indicates the comparison of the tensile force at the measuring points on the geotextile of the groups H1, H2, P1, and P4 when $L = 2.0B$. The four curves of the tensile force show a similar trend. The values of the subsidence area is much larger than the stable area. With the increase of the horizontal distance from the subsidence area, the values decrease rapidly and finally tend to zero.

Figure 4c describes the comparison of the settlement amount of the subsidence area of groups H1, H2, P1, and P4 when $L = 2.0B$. All curves have a peak value in the settlement at the center of the subsidence area. The value of the settlement decreases gradually and is accompanied by the horizontal distance increases, and there is a minimum value when the distance from the center of the subsidence area is 0.75 m. The similar variation trend of the four curves means that the settlement is the largest in the center of the subsidence area, and the settlement is inversely proportional to the horizontal distance of the subsidence area.

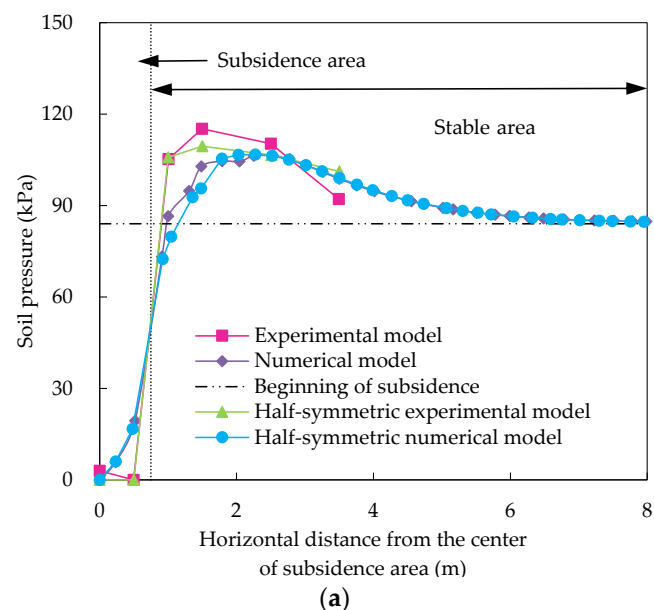
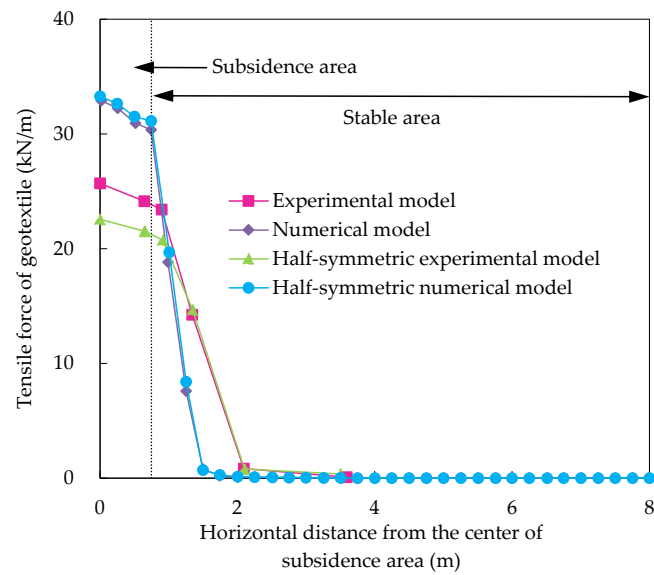
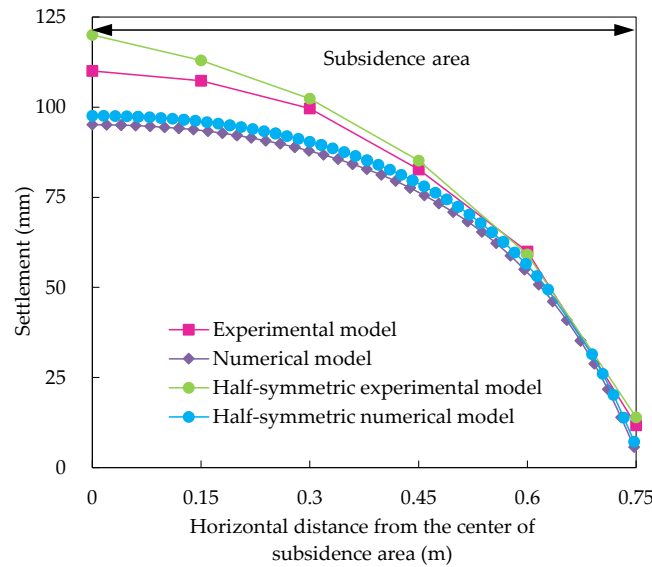


Figure 4. Cont.



(b)



(c)

Figure 4. Comparison between the model test and the numerical model results of the half-symmetric model and the full-section ($L = 2.0B$) at the final state of a subgrade collapse: (a) comparison of the soil pressure curves below the geotextile; (b) comparison of the tensile force curves of the geotextile; (c) Settlement amount of the subsidence area.

3.2. Analysis of the Soil Pressure

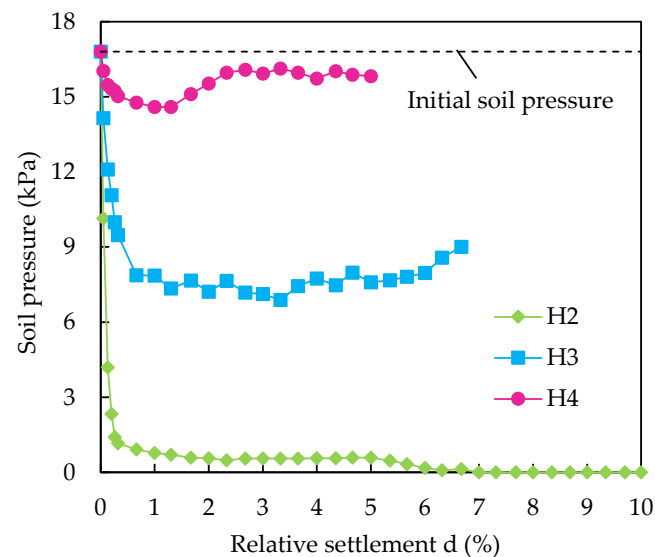
In order to uniformly express the soil settlement for the different subsidence widths, Wu et al. [27] proposed the relative settlement d , as shown in Equation (1).

$$d = (S/B)100, \tag{1}$$

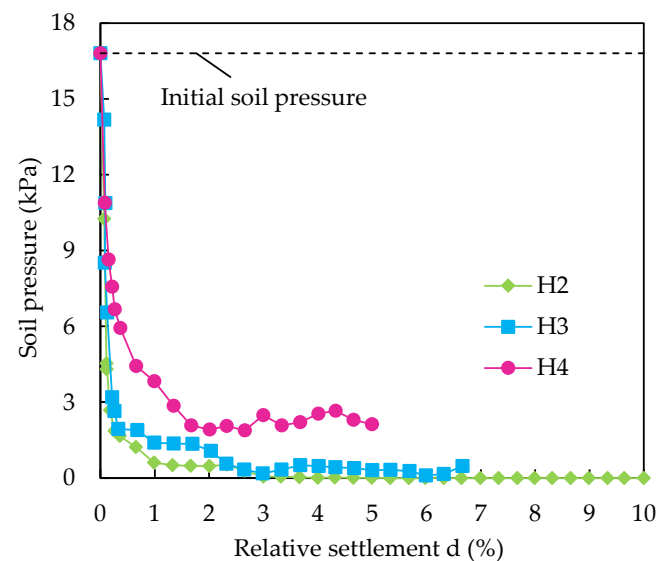
d represents the relative settlement, S represents the soil settlement, and B represents the subsidence width and the units are %, m and m, respectively.

Figure 5 shows the variation of the soil pressure of the half-symmetric model H2-H4 groups within the subsidence area. Each curve is roughly divided into two stages. The steep-dropping stage occurs at $d = 0-0.33\%$, and the soil pressure of each curve of the subsidence area decreases rapidly. The soil pressure of the subsidence area is small when $d = 0.33-10\%$, which is classified as a gentle-change stage. The tensile failure of the geotextile of the

half-symmetric model H3 and H4 groups occur at the relative settlement $d = 6.7\%$ and $d = 5.1\%$, respectively.



(a)



(b)

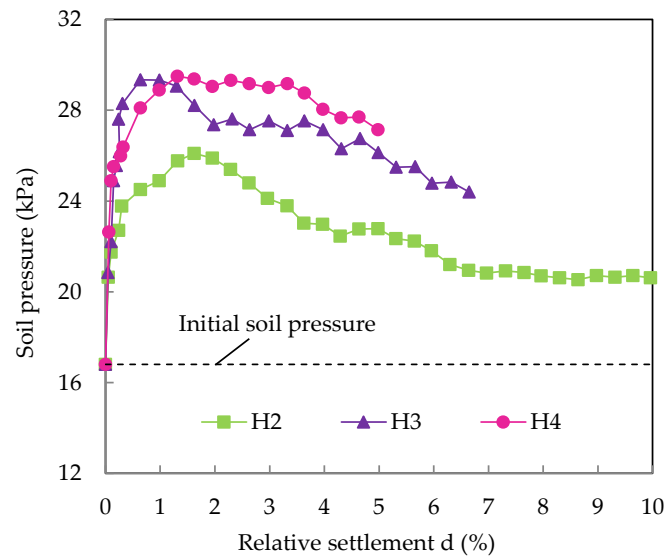
Figure 5. Change of soil pressure of the subsidence area: (a) soil pressure variation curve of the location of T1 with the relative settlement; (b) soil pressure variation curve of the location of T2 with the relative settlement.

Figure 5a shows that the soil pressure variation curve of the location of T1 within the subsidence area. The soil pressure of the H2 group under the gentle-change stage decreases to 0 kPa when $d = 7\%$, which indicates the geotextile separated from the movable bottom plate, at this moment. The membrane pulling effect is fully achieved and the geotextile is controlling the subgrade collapse. The soil pressure of the H3 and H4 groups are about 7.8 kPa and 15.9 kPa, respectively, so the movable bottom plate still bears a certain amount of soil pressure, and the membrane pulling effect of the geotextile has not been fully developed.

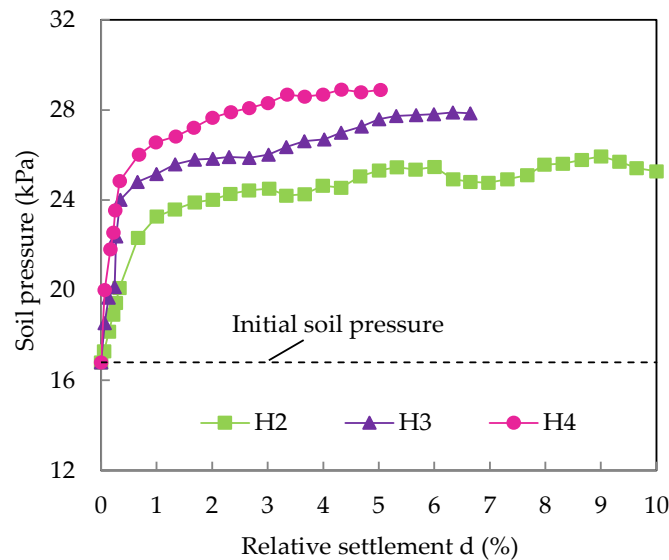
The soil pressure variation curve of the location of T2 within the subsidence area is shown in Figure 5b. With the relative settlement increases, the soil pressure of each curve under the gentle-change stage gradually decreases. The relative settlement corresponding

to the location of T2 is closer to 0 than the location of T1 in the same group due to the different locations of the two soil pressure sensors. It shows that the relative settlement required for the soil pressure of the location of T2 to approach zero is greater.

Figure 6a shows that the soil pressure variation curve of the location of T3 within the stable area. Each curve has a peak value when $d = 1.0\%$, and then gradually decreases and tends to be stable. Figure 6b shows that the soil pressure variation curve of the location of T4 within the stable area. The soil pressure of the location of T4 has different peak values. Comparing with the location of T3, the soil pressure of the location of T4 increases before the soil pressure tends to be stable. When $d = 0-1\%$, with the larger subsidence width, the growth rate becomes greater.



(a)



(b)

Figure 6. Change of soil pressure of the stable area: (a) soil pressure variation curve of the location of T3 with the relative settlement; (b) soil pressure variation curve of the location of T4 with the relative settlement.

The soil pressure of the location of T3 shows a decreasing trend and the soil pressure of the location of T4 shows an increasing trend when $d = 1\text{--}5\%$, which indicates the load is transferred from the location of T3 to the location of T4 within the stable area and the pulling effect of the geotextile is further developed.

3.3. Analysis of the Geotextile of the Tensile Force

Figure 7 shows the strain variation curve of the strain gauges of the locations of Y1, Y3, Y4, and Y6 of the geotextile in each group. In the H3 and H4 groups, the data of the test geotextile are listed before any failure, and the strain gauge sensor are not working when d is greater than 6.7% and 5.1%, respectively. The data of the location of Y1 at the center within the subsidence area and the location of Y3 at the boundary within the subsidence area are larger than the location of Y4 and the location of Y6 within the stable area. The slight change of the location of Y6 of the tensile force of the geotextile indicates that the tensile properties of the geotextile of the location of Y6 are not fully developed. The maximum tensile force of the geotextile of H2-H4 groups is the location of Y3, and the larger the subsidence width is, the larger the tensile force is. For $d = 0\text{--}5\%$, the values of the strain gauges at each position of the H2-H4 groups (except for the location of Y6) increase rapidly, which shows that the membrane pulling effect is fully observed. When $d = 5\text{--}10\%$, the values of the strain gauges at each position of the H2 tends to be stable, the strain gauges at each position of the H3 group still shows an increasing trend and then rapid failure, the strain gauges at each position of the H4 group failed when $d = 5.1\%$. It indicates that the geotextile of the H3 and H4 groups are pulled out or stretched during the test and the geotextile is prone to damage when used to control the settlement with a large subsidence width.

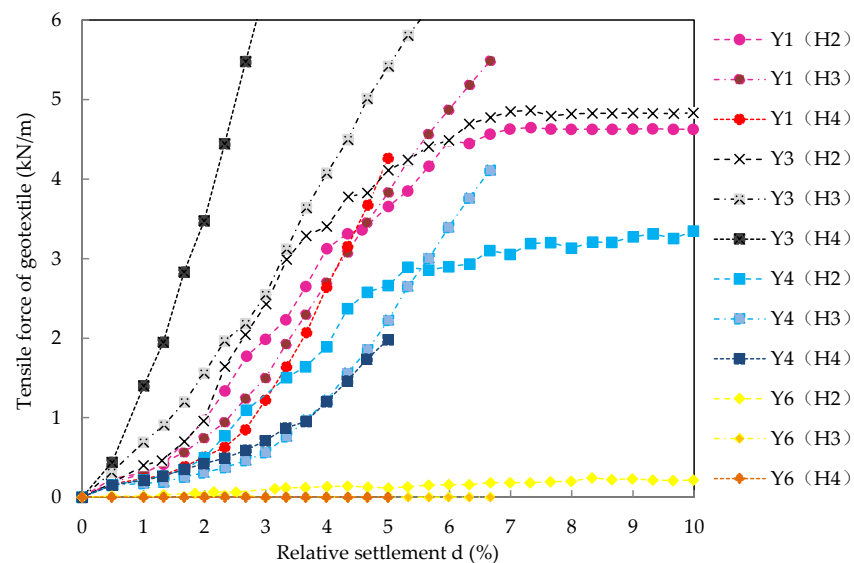
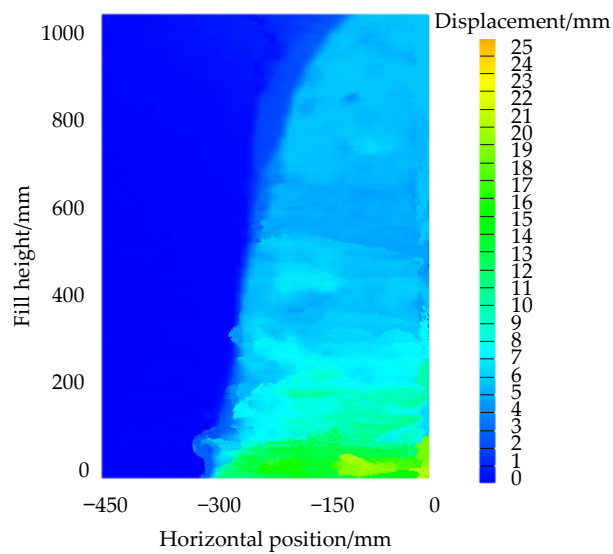


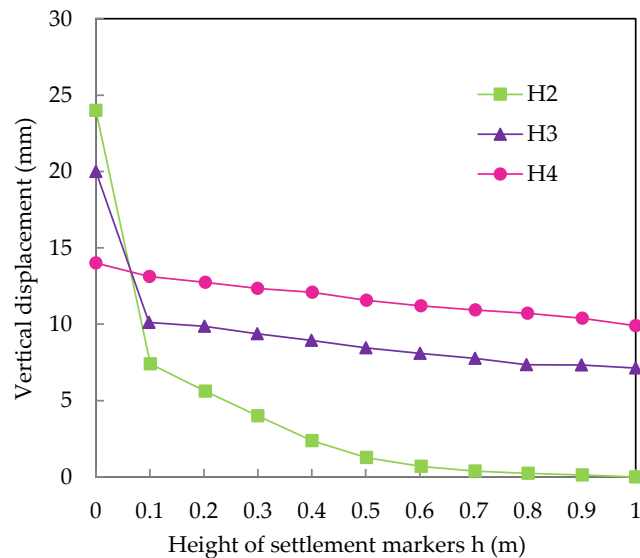
Figure 7. Effect of the subsidence width on the tensile force of the geotextile.

3.4. Analysis of Soil Displacement

The settlement of the soil is observed by the PIV, Figure 8a shows that the displacement contour obtained by the PIV when the relative settlement $d = 5\%$ of the H3 group. Eleven position points of $h = 0.0, 0.1, \dots, 1.0$ m of the center line of the subsidence area are used as reference points for vertical displacement of the soil.



(a)



(b)

Figure 8. Effect of the subsidence width on the soil displacement: (a) vertical displacement cloud image of the soil; (b) vertical displacement curves with different soil heights.

Figure 8b shows the comparison of the vertical displacement curves at the different soil heights on the center line of each model at the end of the settlement. The vertical displacement of the soil of each group has a maximum value at $h = 0$ m and decreases gradually with the increase of h , which indicates the vertical displacement of the soil is transmitted from bottom to top. When $h = 0.2$ m, the maximum vertical displacement of the H4 group is 12.75 mm and the minimum vertical displacement of the H2 group is 5.62 mm, which is 56% lower than the H4 group. The results show that the vertical displacement of each group is different at the same soil height, which decreases with the decrease of the subsidence width. The vertical displacement of the soil of group H2 at $h = 0.8$ m is close to zero, indicating that the influence height of the soil vertical displacement of group H2 within the subsidence area is 0.8 m. When $h = 1.0$ m, the vertical displacement of the soil of the H3 and H4 groups are 7.12 mm and 9.89 mm, respectively. It indicates that the influence height of the soil has not been reached, which is related to the early tension failure of the geotextile. It shows that using the geotextile can effectively control the upward development of the vertical displacement of the soil. Based on the observation, when the settlement with a large subsidence width

is treated, it is suggested to choose a geotextile with a large tensile stiffness to prevent the geotextile from being pulled and damaged in advance.

4. Effect of the Subsidence Width in the Numerical Model

Numerical models P1–P10, having L/B of 4.0, 2.0, 1.0, 4.0, 3.33, 2.86, 2.50, 2.22, 2.0, and 1.0, respectively, are used to study the effect of the subsidence width on the geotextile control of the subgrade collapse. Among the ten models, the numerical models P2 and P9 with an anchorage ratio, L/B of 2.0 and the two models with an anchorage ratio, L/B of 1.0 failed.

This may be caused by the pulling out of the geotextile or the failure of the soil, which is similar with the observed phenomenon of the test, so the geotextile may not be suitable for the subgrade collapse treatment when $L \leq 2.0B$ under the condition of a constant anchorage length.

4.1. Analysis of the Soil Pressure

Figure 9 shows the soil pressure distribution of the geotextile in the stable area for different subsidence widths. All of the curves have a peak value at the boundary between the stable area and the subsidence area, and then decreases rapidly to a smaller value. All of the curves have a second peak value of the soil pressure when the horizontal distance from the center is about 1.35–2 m. The peak value increases with the increase of the subsidence width. The maximum soil pressure value is 1485.27 kPa at the edge of the subsidence area when the anchorage ratio of $L = 2.22B$, and the maximum soil pressure value is 136.65 kPa in the stable area when the anchorage ratio of $L = 2.50B$. The soil pressure of each curve gradually decreases to be stable when the horizontal distance from the center is about 2.25 m. It indicates that the normal stress at the boundary between the stable area and the subsidence area increases significantly and the maximum soil pressure of the stable area does not fluctuate greatly with the increase of the subsidence width. This means that more soil loads in the subsidence area are transferred to the stable area.

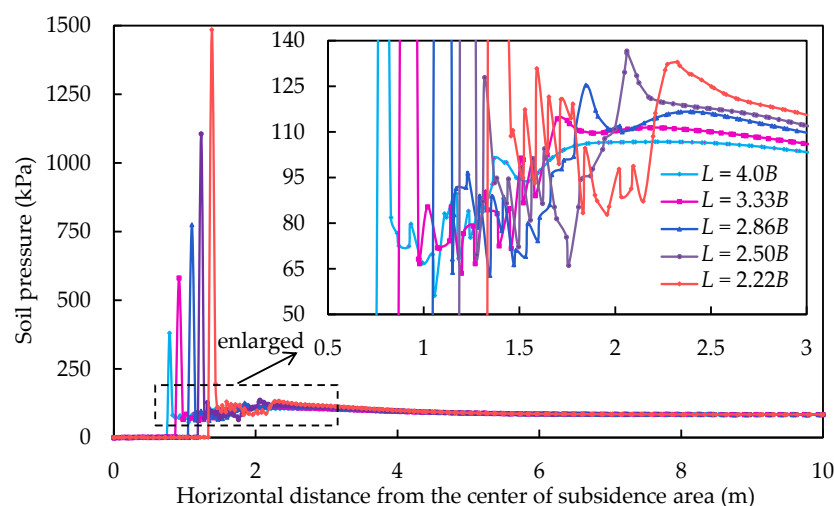


Figure 9. Vertical normal pressure distribution below the geotextile with different subsidence widths.

The subsidence width has less influence on the soil pressure curve of the stable area, while the influence is much greater in the area close to the subgrade collapse edge, and the larger the subsidence width is, the greater the influence of the subsidence width is.

4.2. Analysis of the Geotextile of the Tensile Force

Figure 10 is the tensile force distribution for the full section which is derived from the half-symmetric model. In the subsidence area, the curves with different subsidence widths have similar variation trends, and the tensile force value of the geotextile in the central part of the subsidence area is larger than both sides and gradually decreases to the edge of the subsidence area. In the stable area, the tensile force drops rapidly to zero. It is found that

the tensile force of all of the curves increases with the increase of the subsidence width, and the maximum tensile force appears at the center of the subsidence area, which indicates the center of the subsidence area bears the greatest soil load. The zero tensile force position moves backward with the increase of the subsidence width, indicating that the tensile force transfer range increases with the increase of the subsidence width.

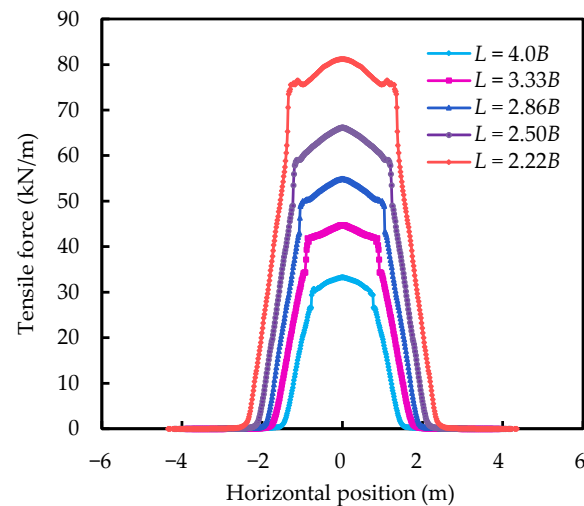


Figure 10. Tensile force distribution of the geotextile for the different subsidence widths.

Figure 11 shows the distribution for the full section which is derived from the half-symmetric model. The maximum value of all of the curves are located at the center of the subsidence area and the vertical deflection of the geotextile increases proportionally with the increase of the subsidence width, the overall shape is “circular-arc”. The vertical deflection for the anchorage ratio of $L = 2.22B$ is the greatest, indicating that the large subsidence width may lead to the instability of the geotextile structure. The tensile strength of the geotextile is an important parameter to indicate the performance of the geotextile. When a subgrade collapse occurred, the geotextile was deformed by a downward tension, the soil load was transferred to the stable area, and the tension-membrane effect may then occur. With the increase of the subsidence width, the geotextile was subjected to a greater load transfer from the soil, which had a side effect on the stability of the structure. It is expected that the geotextile with the greater tensile strength will be required to control the subgrade collapse when the subsidence width is greater, based on the data in this paper.

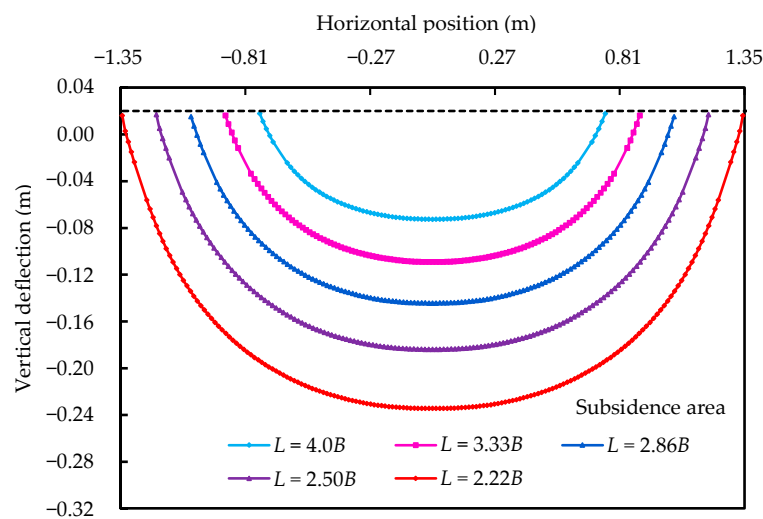


Figure 11. Vertical deflection distribution of the geotextile in the subsidence area for the different subsidence widths.

4.3. Analysis of the Soil Displacement

Figure 12 shows the soil displacement contours of the different subsidence widths. The comparison shows that the anchorage ratios of $L = 4.0B$, $L = 3.33B$, $L = 2.86B$, $L = 2.50B$, and $L = 2.22B$ (See Figure 12a–e), when the anchorage length is unchanged and the width of the subsidence area increases, the value of the vertical soil displacement at the bottom of the subsidence area increases accompanied by increasing the subsidence width. This indicates that the increase of the subsidence width promotes the increase of the soil displacement at the bottom of the subsidence area. The vertical soil displacement legend is shown at the right side of each cloud image. The maximum value of the soil displacement is at the bottom right of the subsidence area in each image, and the displacement occurs along the height. The soil displacement above the subgrade collapse shows an obvious “semi-ellipse” shape, which indicates that the geotextile in the subsidence area deforms downward after the soil moves downward, and the soil arch forms due to the small differential subgrade collapse which is helpful to reduce the soil displacement in the stable area.

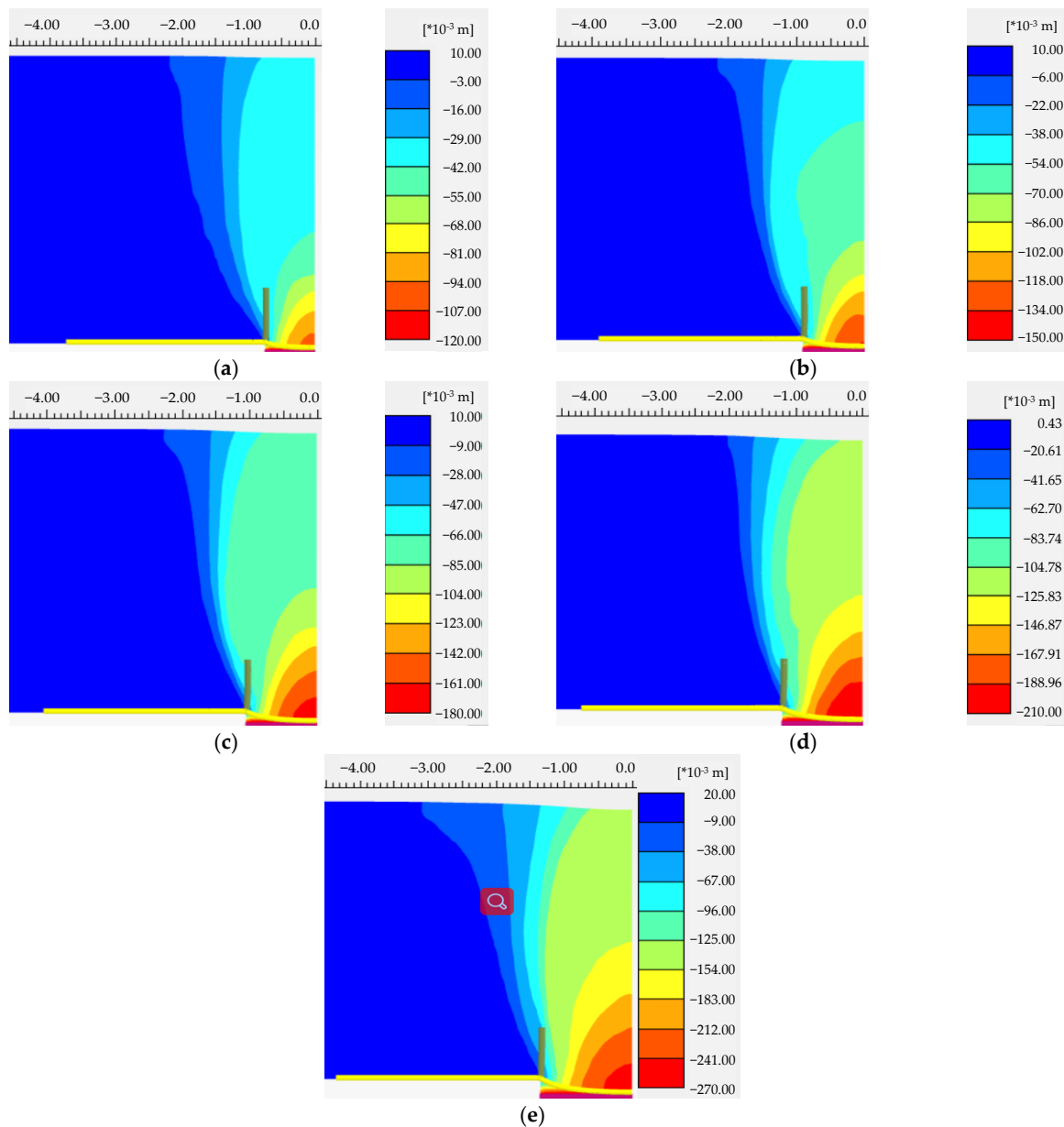


Figure 12. Vertical displacement cloud image of the soil at the final state of the subgrade collapse for the different subsidence widths: (a) $L = 4.0B$; (b) $L = 3.33B$; (c) $L = 2.86B$; (d) $L = 2.50B$; (e) $L = 2.22B$.

Figure 13 is the vertical displacement of the surface distribution for the full section which is derived from the half-symmetric model. Each curve has a vertical settlement peak in the central position of the subsidence area and the settlements at other positions are symmetric around the central position.

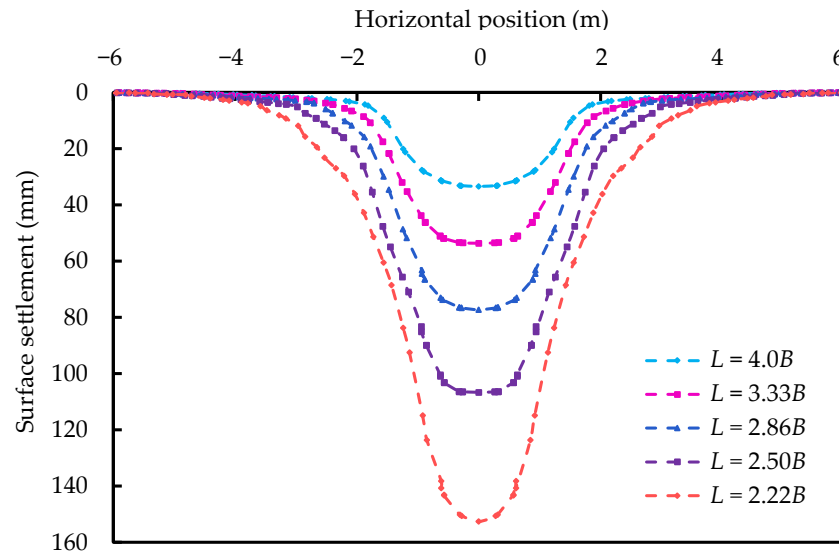


Figure 13. Vertical displacement of the surface of the soil for different subsidence widths.

According to the BS 8006 [34], the ratio of the maximum subgrade collapse of the subgrade surface ds to the deformation range of the pavement Ds should be limited to 1%. The maximum subsidence with the anchorage ratios of $L = 4.0B$, $L = 3.33B$, $L = 2.86B$, $L = 2.50B$ and $L = 2.22B$ at the surface are shown in Table 5. The maximum subgrade collapse of all of the groups is smaller than the specified value of ds/Ds of 1% in BS 8006.

Table 5. Settlement of the subgrade surface with the various anchorage ratios.

Anchorage Ratio, L/B	Maximum Subgrade Collapse, ds (mm)	Deformation Range of the Pavement, Ds (m)	The Ratio of the Maximum Subgrade Collapse to the Deformation Range of Pavement, ds/Ds
4.0	33.46	12.24	0.27%
3.33	53.59	12.42	0.43%
2.86	77.24	13.04	0.59%
2.50	106.64	13.34	0.80%
2.22	152.57	17.44	0.87%

The geotextile plays an important role in the treatment of the subsidence area. Overall, the subsidence width of the geotextile is a key factor. When geotextiles are used to treat a subgrade collapse of a subgrade collapse with the subsidence width of an anchorage ratio for $L \leq 2.0B$, the geotextile will break or the soil structure will have a subgrade collapse, leading to the instability of the treated structure, which is consistent with the laboratory test results.

5. Conclusions

In this paper, to explore the effect of the subsidence width on engineering problems of the geotextile treatment of a subgrade collapse, the half-symmetric model test has been established as well as numerical models. By comparing the full-section model test results with the half-symmetric model results, it proves that the half-symmetric model could represent the full-section model test. In addition, the optimized subsidence width was explored with ten different conditions conducted by numerical models to make up for the deficiencies of the model test work. The influence of the subsidence width on the soil

pressure, the tensile force of the geotextile, and the settlement were analyzed. The main conclusions are as follows.

The test data show a good consistency between the results obtained with the two models. The variation of the data curve for the half-symmetric model and the full-section model test are similar, which verifies the rationality of the half-symmetric model test. The numerical model results of the soil pressure, the tensile force of the geotextile and the soil displacement are consistent with the full-section model tests, which proves the validity of the numerical model.

The subsidence width is an important parameter for the performance that geotextile does to treat a subgrade collapse. With the increase of the subsidence width, more loads of the subsidence area are transferred to the stable area through the geotextile, the vertical normal stress at the edge increases rapidly, the tensile force of the geotextile and the vertical soil displacement in the subsidence area increase substantially. It indicates that the geotextile treatment of a subgrade collapse is not suitable for projects with an anchorage ratio of $L \leq 2.0B$. This recommendation for the geotextile control of a subgrade collapse solely based on the laboratory test, representing the minimum length for the geotextile treatment. The real area, shape, and depth of the subgrade collapse are different from the situation of a simulated subgrade collapse in the laboratory. More research needs to be conducted for the engineering practice application.

Author Contributions: Conceptualization and methodology, D.W. and J.W.; software and validation, Y.L. and J.W.; writing—original draft preparation, Y.L.; writing—review and editing, Y.Y. and D.W.; supervision, D.W. and Y.Y. All authors have read and agreed to the published version of the manuscript.

Funding: This research was supported by the National Natural Science Foundation of China Grant (No. 42067044) and the Natural Science Foundation of Guangxi Grant (No. 2022GXNSFBA035569).

Institutional Review Board Statement: Not applicable.

Informed Consent Statement: Not applicable.

Data Availability Statement: Not applicable.

Conflicts of Interest: The authors declare no conflict of interest.

References

1. Yan, F.Y.; Qiu, W.G.; Sun, K.G.; Jiang, S.H.; Huang, H.Y.; Hong, Y.Q.; Hou, Z.H. Investigation of a large ground collapse, water inrush and mud outburst, and countermeasures during subway excavation in Qingdao: A case study. *Tunn. Undergr. Space Technol.* **2021**, *117*, 104127. [[CrossRef](#)]
2. Song, K.I.; Cho, G.C.; Chang, S.B. Identification, remediation, and analysis of karst sinkholes in the longest railroad tunnel in South Korea. *Eng. Geol.* **2012**, *135*, 92–105. [[CrossRef](#)]
3. Carbonel, D.; Rodriguez-Tribaldos, V.; Gutierrez, F.; Galve, J.P.; Guerrero, J.; Zarroca, M.; Roque, C.; Linares, R.; McCalpin, J.P.; Acosta, E. Investigating a damaging buried sinkhole cluster in an urban area (Zaragoza city, NE Spain) integrating multiple techniques: Geomorphological surveys, DInSAR, DEMs, GPR, ERT, and trenching. *Geomorphology* **2014**, *229*, 3–16. [[CrossRef](#)]
4. Zhou, W.F.; Lei, M.T. Summary editorial for karst hydrogeology: Advances in karst collapse studies. *Environ. Earth Sci.* **2018**, *77*, 803. [[CrossRef](#)]
5. Zhang, N.; Shen, J.S.; Lin, C.; Arulrajah, A.; Chai, J.C. Investigation of a large ground collapse and countermeasures during mountain tunnelling in Hangzhou: A case study. *Bull. Eng. Geol. Environ.* **2019**, *78*, 991–1003. [[CrossRef](#)]
6. Billi, A.; De Filippis, L.; Poncia, P.P.; Sella, P.; Faccenna, C. Hidden sinkholes and karst cavities in the travertine plateau of a highly-populated geothermal seismic territory (Tivoli, central Italy). *Geomorphology* **2016**, *255*, 63–80. [[CrossRef](#)]
7. Li, B.; Feng, Z.; Wang, G.Z.; Wang, W.P. Processes and behaviors of block topple avalanches resulting from carbonate slope failures due to underground mining. *Environ. Earth Sci.* **2016**, *75*, 694. [[CrossRef](#)]
8. Jiao, Y.Y.; Wang, Z.H.; Wang, X.Z.; Adoko, A.C.; Yang, Z.X. Stability assessment of an ancient landslide crossed by two coal mine tunnels. *Eng. Geol.* **2013**, *159*, 36–44. [[CrossRef](#)]
9. Jones, C.J.F.P.; Cooper, A.H. Road construction over voids caused by active gypsum dissolution, with an example from Ripon, North Yorkshire, England. *Environ. Geol.* **2005**, *48*, 384–394. [[CrossRef](#)]
10. Zhao, P.; Yuan, S.; Li, L.P.; Ge, Q.; Liu, J.; Du, L.H. Experimental study on the multi-impact resistance of a composite cushion composed of sand and geofoam. *Geotext. Geomembr.* **2021**, *49*, 45–56. [[CrossRef](#)]
11. Galve, J.P.; Gutierrez, F.; Guerrero, J.; Alonso, J.; Diego, I. Optimizing the application of geosynthetics to roads in sinkhole-prone areas on the basis of hazard models and cost-benefit analyses. *Geotext. Geomembr.* **2012**, *34*, 80–92. [[CrossRef](#)]

12. Keller, G.R. Application of geosynthetics on low-volume roads. *Transp. Geotech.* **2016**, *8*, 119–131. [[CrossRef](#)]
13. Zornberg, J.G.; Azevedo, M.; Sikkema, M.; Odgers, B. Geosynthetics with enhanced lateral drainage capabilities in roadway systems. *Transp. Geotech.* **2017**, *12*, 85–100. [[CrossRef](#)]
14. Rehman, Z.U.; Khalid, U. Reuse of COVID-19 face mask for the amelioration of mechanical properties of fat clay: A novel solution to an emerging waste problem. *Sci. Total Environ.* **2021**, *794*, 148746. [[CrossRef](#)]
15. Rehman, Z.U.; Khalid, U. Optimization of COVID-19 face mask waste fibers and silica fume as a balanced mechanical ameliorator of fat clay using response surface methodology. *Environ. Sci. Pollut. Res.* **2022**, *29*, 17001–17016. [[CrossRef](#)]
16. Bricancon, L.; Villard, P. Design of geosynthetic-reinforced platforms spanning localized sinkholes. *Geotext. Geomembr.* **2008**, *26*, 416–428. [[CrossRef](#)]
17. Villard, P.; Gourc, J.P.; Giraud, H. A geosynthetic reinforcement solution to prevent the formation of localized sinkholes. *Can. Geotech. J.* **2000**, *37*, 987–999. [[CrossRef](#)]
18. Fu, H.Y.; Yin, M.M.; He, W. Study of design theory of geosynthetics for treating road sinkhole collapse hazard in karst terrain. *Rock Soil Mech.* **2011**, *32*, 2983–2988. (In Chinese)
19. Mehrjardi, G.T.; Khazaei, M. Scale effect on the behaviour of geogrid-reinforced soil under repeated loads. *Geotext. Geomembr.* **2017**, *45*, 603–615. [[CrossRef](#)]
20. Huckert, A.; Briancon, L.; Villard, P.; Garcin, P. Load transfer mechanisms in geotextile-reinforced embankments overlying voids: Experimental and analytical approaches. *Geotext. Geomembr.* **2016**, *44*, 442–456. [[CrossRef](#)]
21. Eekelen, S.J.M.V.; Bezuijen, A.; Lodder, H.J.; Tol, A.F.V. Model experiments on piled embankments. Part I. *Geotext. Geomembr.* **2012**, *32*, 69–81. [[CrossRef](#)]
22. Chawla, S.; Shahu, J.T. Reinforcement and mud-pumping benefits of geosynthetics in railway tracks: Model tests. *Geotext. Geomembr.* **2016**, *44*, 366–380. [[CrossRef](#)]
23. King, D.J.; Bouazza, A.; Gniel, J.R.; Rowe, R.K.; Bui, H.H. Serviceability design for geosynthetic reinforced column supported embankments. *Geotext. Geomembr.* **2017**, *45*, 261–279. [[CrossRef](#)]
24. Villard, P.; Huckert, A.; Briancon, L. Load transfer mechanisms in geotextile-reinforced embankments overlying voids: Numerical approach and design. *Geotext. Geomembr.* **2016**, *44*, 381–395. [[CrossRef](#)]
25. Huckert, A.; Garcin, P.; Villard, P.; Briancon, L.; Auray, G. Experimental and numerical approaches of the design of geotextile reinforced embankments prone to sinkholes. In Proceedings of the 10th International Conference on Geosynthetics, Berlin, Germany, 21–25 September 2014.
26. Briancon, L.; Villard, P.; Chevalier, B. New developments in the modeling and the design of geosynthetic reinforcements of platforms subjected to localized sinkholes. In Proceedings of the Advances in Analysis, Modeling & Design, GeoFlorida, West Palm Beach, FL, USA, 20–24 February 2010; pp. 664–671.
27. Wu, D.; Luo, C.; Li, Y.K.; Yang, Y.X.; Liang, Y.H.; Wu, J.J. Application of a geotextile in the treatment of post-subsidence in Karst Areas. *Appl. Sci.* **2021**, *11*, 11826. [[CrossRef](#)]
28. Zhang, J.; Liu, S.W.; Pu, H.F. Evaluation of an improved technique for geosynthetic-reinforced and pile-supported embankment. *Adv. Mater. Sci. Eng.* **2015**, *2015*, 612760. [[CrossRef](#)]
29. Feng, S.Y.; Xu, R.Q.; Cheng, K.; Yu, J.L.; Jia, Q.J. Centrifuge model test on the performance of geogrid-reinforced and pile-supported embankment over soft soil. *Soil Mech. Found. Eng.* **2020**, *57*, 244–251. [[CrossRef](#)]
30. Wu, D.; Wu, J.J.; Xu, C.; Chen, X.J.; Huang, X. Model test of geotextiles in controlling the collapse of karst roadbed. *Rock Soil Mech.* **2020**, *41*, 1–11. (In Chinese)
31. Wu, D.; Luo, C.; Wu, J.J. Model tests of geotextile in collapse treatment of karst subgrade. In Proceedings of the 6th International Conference on Hydraulic and Civil Engineering, Xi'an, China, 11–13 December 2020; Volume 643, p. 012058.
32. Wu, D.; Liang, Y.H.; Luo, C.; Wu, J.J. Influence of collapse width on the effect of geotextile in controlling subgrade collapse based on symmetrical semisection model tests. In Proceedings of the 6th International Conference on Hydraulic and Civil Engineering, Xi'an, China, 11–13 December 2020; Volume 643, p. 012006.
33. Wang, L.P.; Zhang, G.; Zhang, J.M. Centrifuge model tests of geotextile-reinforced soil embankments during an earthquake. *Geotext. Geomembr.* **2011**, *29*, 222–232. [[CrossRef](#)]
34. *British Standard 8006*; Code of Practice for Strengthened/Reinforced Soils and Other Fills. British Standard Institution: London, UK, 2010.